Author version: *Clim. Dyn., vol.40(3-4); 2013; 743-759*

Interannual variability of the Tropical Indian Ocean mixed layer depth

Keerthi, M.G.[1], M. Lengaigne[1 2], J.Vialard[2], C. de Boyer Montégut[3], P.M. Muraleedharan[1]

1. National Institute of Oceanography, CSIR, Goa, India

2. Laboratoire d'Océanographie Expérimentation et Approches Numériques, CNRS, UPMC, IRD, Paris, France

3. Laboratoire d'Océanographie Spatiale, IFREMER, Brest, France

Revised for *Climate Dynamics:* January 2012

Corresponding author address:

Keerthi M.G.

Physical Oceanography Division, National Institute of Oceanography, Dona Paula. Goa.

India – 403004; E-mail: keerthanaamg@gmail.com

Abstract

In the present study, interannual fluctuations of the mixed layer depth (MLD) in the tropical Indian Ocean are investigated from a long-term (1960-2007) eddy permitting numerical simulation and a new observational dataset built from hydrographic in-situ data including Argo data (1969-2008). Both datasets show similar interannual variability patterns in relation with known climate modes and reasonable phase agreement in key regions. Due to the scarcity of the observational dataset, we then largely rely on the model to describe the interannual MLD variations in more detail. MLD interannual variability is two to four times smaller than the seasonal cycle. A large fraction of MLD interannual variations is linked to large-scale climate modes, with the exception of coastal and subtropical regions where interannual signature of small-scale structures dominates. The Indian Ocean Dipole is responsible for most variations in the 10°N-10°S band, with positive phases being associated with a shallow MLD in the equatorial and south-eastern Indian Ocean and a deepening in the south-central Indian Ocean. The El Niño signature is rather weak, with moderate MLD shoaling in autumn in the eastern Arabian Sea. Stronger than usual monsoon jets are only associated with a very modest MLD deepening in the southern Arabian Sea in summer. Finally, positive Indian Ocean Subtropical Dipoles are associated with a MLD deepening between 15°S and 30°S. Buoyancy fluxes generally appear to dominate MLD interannual variations except for IOD-induced signals in the south-central Indian Ocean in autumn, where wind stirring and Ekman pumping dominate.

Keywords: Mixed layer, interannual variability, Indian Ocean, Indian Ocean Dipole, El Niño/Southern Oscillation, Monsoon.

1. Introduction

Almost any ocean profile displays homogeneous temperature, salinity and density in the upper oceanic layer. This homogeneous layer results from active vertical mixing near the surface, promoted by various processes like wind-stirring, waves, turbulence generation by vertical shear or night time convective mixing. The mixed layer is extremely important in establishing the world ocean's mean state and variability, as it acts as an interface between the atmosphere and interior ocean. Water masses acquire their properties within the mixed layer in deep-water formation and subduction regions. The mixed layer thickness also modulates its heat capacity, and hence its propensity to be heated or cooled by atmospheric forcing. In this respect, the mixed layer is an essential parameter in air-sea interactions, because it modulates the amplitude of the sea surface temperature (hereafter SST) response.

Numerous studies have already investigated seasonal variations of the mixed layer depth (hereafter MLD) in the Indian Ocean. Special attention has been paid to the northern Indian Ocean, which exhibits a prominent MLD semi-annual cycle, associated with the seasonally reversing monsoonal circulations (Schott et al. 2002). MLD seasonal variability has been extensively studied over the Arabian Sea using both in situ observations (Rao et al. 1989, Rao and Sivakumar 2003, Sreenivas et al. 2008) and model simulations (Prasad 2004, de Boyer Montegut et al. 2007, McCreary et al. 1989). During summer monsoon, the MLD increases markedly in the interior Arabian Sea owing to Ekman convergence associated with the Findlater jet (Findlater 1969) and shallows west of the Jet axis. During winter monsoon, negative buoyancy fluxes play a major role in the convective deepening of the MLD. In contrast, inter-monsoon seasons (spring and autumn) are characterized by weaker winds along with strong incoming solar radiation that result in a thin and warm mixed layer. Compared to the Arabian Sea, the Bay of Bengal exhibits weaker seasonal MLD variations (Gopalakrishna et al. 1988, Rao et al. 1989, Shenoi et al. 2002, Prasad 2004, Babu et al. 2004, Narvekar and Kumar 2006). This is especially true in the northern part of the Bay where strong salinity stratification prevents convective cooling. The southern part of the Bay however shows a distinct semi-annual variability with deep MLDs during summer and winter monsoons and shallow MLDs during spring and autumn intermonsoons, as for the Arabian Sea. Wind-driven mixing largely controls this seasonal variability (Narvekar and Kumar 2006). At the equator, the Wyrtki Jet (Wyrtki 1973) that develops during autumn results in downward sloping of MLD from west to east (Ali and Sharma 1994, Brien and Hurlburt 1974), while excess of precipitation in winter results in the formation of a barrier layer west of Sumatra, shoaling the MLD (Masson et al. 2002, Qu and Meyers 2005, Du et al. 2005). The seasonal cycle in the southern tropical Indian Ocean has been less

investigated. Seasonal shoaling and deepening of the mixed layer in the south-western Tropical Indian Ocean has been related to annual cycle of the wind, through its stirring effect and its impact on buoyancy fluxes and thermocline depth (Foltz et al. 2010).

To our knowledge, Carton et al. (2008) is to date the only study that maps interannual MLD variations at global scale from observations. Their study provides little details about the Indian Ocean. They show that interannual MLD variability in boreal summer is confined to the Arabian Sea and mainly driven by changes in the strength of the monsoonal winds. In contrast, they relate interannual MLD variations during boreal winter to remote forcing from the Tropical Pacific. The Pacific Ocean is indeed home to the most powerful climate variation at interannual timescales on the planet: the El Niño-Southern Oscillation (hereafter, ENSO; see e.g. Wang and Picaut 2004, McPhaden et al. 2006). During an El Niño, air-sea interactions promote the growth of a positive SST anomaly in the central and eastern Pacific that usually peaks at the end of the year. Teleconnections associated with El Niño result in an overall warming of the Indian Ocean (e.g. Klein et al. 1999). Carton et al. (2008) suggest that those atmospheric teleconnections induce a MLD shoaling in the eastern equatorial Indian Ocean and a deepening south of the equator in the central basin during El Niño events.

The Indian Ocean has long been viewed as largely passive, with interannual variations arising from remote forcing of ENSO, as suggested above. In the recent years, this vision has deeply changed (e.g. Schott et al. 2009). First, local air-sea interactions allow ENSO remotely forced SST anomalies and their climatic impacts to persist in the Indian Ocean well beyond the end of El Niño (Xie et al. 2010). In addition, the Indian Ocean is home to indigenous modes of variability. The Indian Ocean Dipole (hereafter IOD) is, like ENSO, the result of air-sea interactions. The IOD peaks in autumn, and is associated with anomalous easterlies in the central Indian Ocean, cold SST anomalies close to Java and Sumatra, and warm SST anomalies in the western Indian Ocean (e.g. Saji et al. 1999, Webster et al. 1999, and Murtugudde et al. 2000). There is a tendency of IODs to be triggered by El Niño events, but they can also occur independently (e.g. Annamalai et al. 2003). There is another recurrent climate variability that is also characterized by a zonal temperature dipole further south: the Subtropical Indian Ocean Dipole (hereafter SIOD, Behera and Yamagata 2001). It is characterized by SST anomalies of opposite polarities west of Australia and South-East of Madagascar that peak in austral summer. Unlike ENSO and the IOD, SIOD development appears to be largely related to air-sea fluxes and not driven by oceanic dynamical processes.

MLD is a crucial parameter in air-sea interactions. A thick MLD has a larger heat capacity, and is hence less responsive to atmospheric heat fluxes. Air sea flux variations are important for most of

the Indian Ocean climate variations mentioned above. They are responsible of the Indian Ocean warming during ENSO (e.g. Klein et al. 1999) and its maintenance after the end of ENSO (Xie et al. 2010), of the development of the SIOD (Behera and Yamagata 2001), can contribute either positively or negatively to IOD growth depending on the season and location (Hendon 2003, Murtugudde et al. 2000) and damp the amplitude of summer monsoon interannual fluctuations (Ju and Slingo, 1995). For these reasons, it is important to document and understand interannual variations of the mixed layer depth associated with those climate modes in the Indian Ocean. There is however to our knowledge only one paper describing interannual variations of the MLD (Carton et al. 2008), and with no specific focus on the Indian Ocean.

In this paper, we describe the mixed layer depth interannual variability in the Indian Ocean and relate it to the known climate modes affecting its variability, using both available observations and a general circulation model. In section 2, we describe the observational estimates and the simulation, as well as our statistical methods. In section 3, we describe the interannual variability of the MLD in the model and observations. Section 4 details MLD patterns associated with each climate mode in the Indian Ocean, and qualitatively discusses processes responsible for MLD interannual variations. The last section summarizes and discusses our results.

2. Data and methods

2.1 Numerical experiment

The numerical simulation used in this study was provided by the DRAKKAR project (Brodeau et al. 2010), and is based on the NEMO (Nucleus for European Modelling of the Ocean, formerly known as OPA) Ocean General Circulation Model (hereafter, OGCM; Madec 2008). The model is based on primitive equations, uses a free surface formulation (Roullet and Madec 2000).

We analyzed two DRAKKAR configurations: a coarse 2° resolution (ORCA-R2) and an eddy permitting ¼° resolution (ORCA-R025). The common vertical grid of these configurations has 46 levels with a 6-m spacing at the surface increasing to 250-m in the deep ocean. Bathymetry is represented with partial steps (Barnier et al. 2006). The large-scale MLD variations from both versions are very similar, and we will only show results for the eddy-permitting version hereafter.

Density is computed from potential temperature, salinity and pressure using the Jackett and McDougall (1995) equation of state. Vertical mixing is parameterized from a turbulence closure scheme based on a prognostic vertical turbulent kinetic equation, which has been shown to perform well in the tropics before (Blanke and Delecluse 1993). Lateral mixing acts along isopycnal surfaces,

with a Laplacian operator and 200 $m^2.s^{-1}$ constant isopycnal diffusivity coefficient (Lengaigne et al. 2003). Shortwave fluxes penetrate into the ocean based on a single exponential profile (Paulson and Simpson 1977) corresponding to oligotrophic water (attenuation depth of 23 m).

The model is forced from 1958 to 2004 with the DFS3 dataset, described in detail by Brodeau et al. (2010). This dataset is essentially based on the corrected ERA-40 re-analysis (and ECMWF operational analyses beyond 2002) for near surface meteorological variables and on the corrected ISCCP-FD radiation product (Zhang et al, 2004) after 1984. No surface temperature restoring is used and salinity is restored to climatological values, with a relaxation time scale of 33 days (for a 10 m thick layer). We did discard the first two years of this simulation (1958-1959) to allow planetary waves to achieve the Indian Ocean basin adjustment: our analyses only cover the 1960-2007 period.

This OGCM has been extensively validated in uncoupled mode with various forcing strategies (e.g. Vialard et al. 2001, Cravatte et al. 2008) and in coupled mode (e.g. Lengaigne et al. 2006, Lengaigne and Vecchi 2010). It accurately simulates equatorial dynamics and basin wide structures of currents, sea level and temperature in the tropics. The particular simulation that we use in this paper also accurately reproduces interannual variations of heat content in the Tropical Pacific (Lengaigne et al. 2011) and of sea level in the Indian Ocean (Nidheesh et al. 2011).

2.2 Observational datasets

Monterey and Levitus (1997) produced a MLD seasonal cycle from temperature and salinity seasonal climatologies. de Boyer Montégut et al. (2004; dBM04 hereafter) pointed out that MLD computation is a non-linear operation, and provided MLD climatology from single-profile MLD estimates. In the present paper, the dBM04 methodology has been applied with some improvements to remove outliers (see hereafter) for producing an interannual MLD product. Our dataset merges classical hydrographic data over 1969-2008, including Argo data over the past decade. Measurements come from following instruments: mechanical bathythermograph (MBT), expendable bathythermograph (XBT), conductivity-temperature-depth (CTD) and profiling floats (PFL). Classical hydrographic data at observed levels are obtained from the National Oceanic Data Center (World Ocean Database 2009, for MBT, XBT, CTD) and from the World Ocean Circulation Experiment (WOCE) 2002 database (CTD and PFL). We also use daily data from moored buoys of the RAMA Indian Ocean array. This results in a total of about 565,000 temperature profiles for the tropical Indian Ocean. Before the beginning of 2000's, Indian Ocean observations mostly relied on XBTs data along voluntary ship lines and on occasional oceanographic cruises. Since the beginning of the Argo program (Gould et al. 2004), individual profiling floats provide a better observational

spatial coverage than for the historical period (Figure 1). The Argo network has reached its target density of observations in late 2006 (Figure 1c).

The recent period hence provides a sufficient spatial and temporal coverage to provide MLD monthly estimates over the entire Indian Ocean using a density criterion. For the Argo period (2002-2008), a MLD dataset (hereafter Argo dataset) can be defined as the depth where the density increase with respect to density at 10 m corresponds to a 0.2° decrease (i.e. a variable density criterion is used). The Argo period is however too short (7 years) to fully describe the MLD interannual variability and will hence mainly be used to investigate the climatological MLD variations. The historical hydrographic data allows describing MLD interannual variations over a longer period (33 years), at the expense of a poorer data spatial coverage, especially in the Southern Indian Ocean and Bay of Bengal (Figure 1) and have only very sparse salinity data. For the entire period (1969-2008), a MLD dataset (hereafter hydrographic dataset) is then computed using a temperature, rather than a density criterion. MLDs are computed as the depth with a 0.2 °C absolute temperature difference from 10m temperature (as in dBM04). Due to its good temporal coverage, this dataset will be used to investigate interannual MLD variations over the past decades. It must however be kept in mind that this observational dataset does not account for salinity variations. For both dataset, MLDs are estimated directly from individual temperature profiles at their native vertical resolution A linear interpolation between levels is then used to estimate MLD. The reference depth is set at 10 m to avoid aliasing by the strong diurnal cycle in the top few meters of the ocean. A new quality control test was added (in comparison with dBM04), in order to reject erroneous MLD estimates. This is important in this relatively sparse data context, because a few outliers can affect the final data quality quite badly. That test basically compares every observation with the seasonal climatology of available observations within a 1000km radius, and rejects about $1/1000^{th}$ of MLD estimates. The data is then reduced on a regular 2° monthly grid, by taking the median of all MLDs in each grid mesh. A slight smoothing is further applied. The last step consists in an optimal prediction of the missing data using ordinary kriging method. This filling was limited to a 1000 km radius disk of every cell point containing at least 5 values, to prevent unrealistic extrapolation as much as possible (see dBM04 for a review). These new observational MLD datasets are available at http://www.lodyc.jussieu.fr/cdblod/mld.html.

In the model, the MLD is calculated online using a 0.01 $kg.m^{-3}$criterion. A 0.2°C threshold corresponds to a 0.03 $kg.m^{-3}$ density change in the surface layer of the tropical Indian Ocean and is hence rather consistent with our model MLD threshold.

For wind stress, we use gridded estimates from the QuikSCAT scatterometer produced at

Centre ERS d'Archivage et de Traitement (CERSAT, Bentamy et al. 2003).

2.3 Methods

When comparing model and observations (Section 3), interannual anomalies are simply calculated by removing the mean seasonal cycle for both datasets. In Section 4, we computed model interannual anomalies by de-seasoning and de-trending 5-day average model outputs using STL decomposition procedure (Cleveland et al. 1990). STL is a filtering procedure for decomposing time series into trend, seasonal and residual components. We used a 7-year threshold for defining the lowest frequency component (i.e. trend), but the results in this paper are robust when using a 5-year cutoff. Results are also robust if interannual anomalies are more simply computed by removing the long-term mean seasonal cycle.

In our eddy-permitting simulation, there is a significant amount of meso-scale MLD variability associated with oceanic eddies, or other small scale features. Since we are mostly interested in large-scale MLD variations related to climate variability, the model MLD is filtered in space to retain only large spatial scales (> 250 km). We do this by applying the iterative application of the heat diffusion equation described in Weaver and Courtier (2001), which is well suited to conduct spatial filtering in domains with complex boundaries, like the ocean.

In order to extract the variability associated with various climate modes, we have used standard indices. In the Pacific, ENSO is classically represented from the averaged SST anomalies over the Nino3.4 (120°W-170°W, 5°N-5°S) region during November-January. The Indian Ocean Dipole (IOD) is represented by the dipole mode index (DMI, Saji et al. 1999) computed as the difference between interannual SST anomalies in the western (50°E-70°E, 10°N-10°S) and eastern (90°E-110°E, 10°S-0°S) equatorial Indian Ocean in September-November. The Subtropical Indian Ocean Dipole (SIOD) is represented by Subtropical Dipole Index (SDI, Behera and Yamagata 2001) computed as the difference between interannual SST anomalies in its eastern (90°E-100°E, 29°S-18°S) and western (55°E-65°E, 37°S-27°S) poles in December-March. The intensity of the Monsoon is represented by a dynamical index (MON) proposed by Webster and Yang (1992) available at http://iprc.soest.hawaii.edu/users/ykaji/monsoon/seasonal-monidx.html and calculated as the vertical wind shear between 850 and 200 hPa in June-August in a box encompassing the Northern Indian Ocean (40°E-110°E; 0°N-20°N). All the indices above have been normalized by their standard deviation. Apart from these indices, we will also use definitions from Ummenhofer et al. (2009) classification to perform composites for IOD / ENSO over the Indian Ocean. Anomalously strong (weak) monsoons are defined as years when the normalized MON seasonal anomalies are larger

(lower) than 0.5.

In order to extract patterns associated with each mode of variability over the Indian Ocean, we use regression techniques. Since we use standardized (adimensional) indices, these regressions provide values in physical units (e.g. meters for MLD), which correspond to the "typical" anomalies associated with an IOD, ENSO, etc… Because of the strong correlation between the IOD and ENSO indices (0.7, see Table 1), it is difficult to isolate the signals associated with each of those climate modes using a simple linear regression. We hence use partial regression to isolate signals purely associated with, e.g., the IOD or ENSO. If one wants to compute the partial regression between, e.g., a time series of MLD M_i and the DMI index D_i independently of the ENSO index E_i, one first subtract signals that are linearly related to E_i from M_i and D_i and perform a regression between the residuals. This technique has already been applied successfully in several studies to separate ENSO and IOD signals (e.g. Yamagata et al. 2004, Yu et al. 2005, Izumo et al. 2010).

The amount of energy transferred from the atmosphere to the mixed layer is proportional to the cube of the friction velocity and surface buoyancy fluxes. These two quantities will be used to qualitatively infer the respective contribution of buoyancy flux and mechanical energy input to interannual MLD variations. The net surface buoyancy B_o is computed as follows:

$$B_o = B_h + B_w$$

$$B_o = \frac{\alpha * Q_o}{C_p} + \beta * (P - E) * S_o$$

Where B_h is the buoyancy due to heat flux, B_w the buoyancy related to fresh water flux, α and β the coefficients of thermal and haline expansion, Q_o the net heat flux, C_p the specific heat of water, P-E the fresh water flux and S_o the surface salinity (Gill 1982). The friction velocity u^* is calculated as:

$$u^* = \sqrt{\frac{\tau}{\rho}}$$

where τ is the surface wind stress and ρ the density of seawater.

3. Model Validation

In this section, we will describe the MLD long-term mean, seasonal cycle and interannual variability from the model and observations.

Figure 2 shows the long-term mean MLD in the model and observational product. There is an overall good agreement of large-scale MLD structures between the model and observations. The

MLD main features south of 10°N are largely linked to the climatological winds, with shallow MLD in the equatorial band (~30 m), due to weak winds (and strong solar flux), deeper MLD between 10°S and 20°S (~30-60 m) where easterlies are strongest. In the northern Indian Ocean, there is a clear contrast between the Bay of Bengal and the Arabian Sea. The mixed layer is deeper in the Arabian Sea, largely because of the very intense monsoon jet in summer (that causes both mixing and downwelling to the right of the jet axis, de Boyer Montégut et al. 2007). Using a MLD criterion based on temperature (Fig. 2a) rather than density (Fig. 2b) give similar results except in the Bay of Bengal and eastern equatorial Indian Ocean where shallower MLDs are obtained when using a density criterion, owing to the strong salinity stratification (river runoffs, intense rainfall during summer monsoon). The model MLD captures those large-scale structures accurately (Fig. 2c), despite a shallower than observed MLD in the equatorial region. This difference may be related to the presence of a thick barrier layer in this region (Qu and Meyers 2005), that is either underestimated by the observational product due to rather sparse observations in the upwelling region (Figure 1) or overestimated in the model.

Figure 3 compares the mean seasonal cycle anomalies with respect to the long term mean in the model and observations. There is an overall MLD deepening in summer driven by the intense summer monsoon winds throughout the basin during the Indian Monsoon. The MLD deepens right of the monsoon jet axis, as a result of Ekman-driven downwelling there. To the left of the monsoon jet, Ekman-driven upwelling results in a weaker MLD deepening. Autumn is mainly characterized by a deep MLD between 10°S and 20°S related to the relatively intense easterlies at this season while MLD shoals slightly in the western Arabian Sea due to weak winds and strong shortwave radiation. During boreal winter, MLD strongly shoals in the southern hemisphere, as a result of weak winds and downward surface heat fluxes in this region. In the Northern Indian Ocean, the negative buoyancy flux brought by the excess of evaporation over precipitation largely explains the relatively deep MLDs in boreal winter (de Boyer Montégut et al. 2007). In spring, weak easterlies in both hemispheres result in a MLD shoaling over most of the tropical Indian Ocean.

Compared to observational estimates, the model performs well during inter-monsoon seasons (spring and autumn) but tends to overestimate the amplitude of the seasonal cycle during both monsoons (summer and winter), especially south of 15°S. In the Northern Indian Ocean, the clearest model bias is a too deep MLD in the Northern Arabian Sea during winter. We found no obvious simple explanation for the model biases.

Figure 4 displays the coefficient of variance (standard deviation of interannual anomalies, divided by the long term mean) for each season, from the observations (Fig 4a-d) and model (Fig 4e-

h). The largest MLD interannual variations occur in autumn and winter in the eastern equatorial Indian ocean (and along Java and Sumatra), and in the central Indian Ocean between the equator and 10°S, reaching up to 40% of the long-term mean value there. Interannual variability appears largely in the same regions in spring, but with smaller amplitudes. In summer and autumn, strong MLD interannual variations are found in the western equatorial Indian Ocean and in the Oman upwelling region.

The broad agreement between the large-scale patterns in the model and observations is a first suggestion that the model captures the main regions of interannual variability of the MLD. The model overestimates the amplitude of the variability in the central Indian Ocean between the equator and 10°S in autumn against the data products. Discrepancies between model and observations may be either linked to model deficiencies or to the very limited data coverage in the observational dataset, especially in the southern hemisphere (Fig. 1).

In order to further validate the modeled MLD interannual variability, Figure 5 provides composites of MLD anomalies for anomalous monsoon years in summer, for IOD years in autumn (when the IOD peaks) and for ENSO years in winter (when ENSO peaks). The paucity of observed data south of 20°S (Figure 1) prevents us to assess the SIOD impact onto MLD variations in observations. The main monsoon related signal in the northern Indian Ocean consists of a slight deepening (~ 2m) of the central and western Arabian Sea and in the eastern Indian Ocean just north of the equator (~ 4m). The model is in general able to simulate these features and the time series of the interannual summer MLD fluctuations in the Arabian Sea are in broad agreement between the model and observations, with a correlation of ~0.6 (Figure 6a). A MLD deepening up to 5m characterizes anomalously strong monsoons (e.g. 1984, 1989) while weaker monsoons usually display a corresponding shoaling (e.g. 1987, 2006). It must however be noted that the amplitude of the interannual MLD signals in the Arabian Sea are modest in both datasets, with an interannual standard deviation that does not exceed ~4m.

Because of the ~0.7 correlation between ENSO and IOD (Table 1), Figure5c-f does not allow to separate signals associated with these two modes of variability, but should nonetheless provide an evaluation of the MLD response to a combined El Nino and positive IOD forcing (the most common occurrence in observations). During a positive IOD, the thermocline shallows in the eastern equatorial Indian Ocean and south of Java and Sumatra (e.g. Murtugudde et al. 2000). There is an associated MLD shallowing in that region in both model and observations. But the clearest signal is seen south of the equator, in the central Indian Ocean. The MLD deepens there; in the same region where Ekman pumping associated with the IOD westerly wind anomalies induce a thermocline

deepening (e.g. Webster et al. 1999). The agreement between the composites from model and observations south of the equator also holds true from one event to another (correlation of ~0.7, Fig. 6b), with the exception of the 1991 positive IOD event where the model display a strong MLD deepening not detected in the observational dataset, model and observations agree well for all major positive and negative IOD events (e.g. 1982, 1994, 1997).

The ENSO composite for winter shows a more pronounced MLD shoaling in the eastern equatorial Indian Ocean and south of Java and Sumatra compared to the IOD autumn pattern. The MLD deepening south of the equator also weakens and propagates westward in both model and observations. In addition, there is a consistent MLD deepening in the southern part of the Bay of Bengal and in the south-eastern Arabian Sea in both datasets. There is a very good phase agreement between MLD interannual variations in the model and observations in both regions (correlation > 0.75, Figure 6cd). The amplitude of the model MLD variability is however about 3 times weaker than in the observations along the Sumatra coast. This mismatch could be related to either our observational dataset that do not take into account the salinity effect in the MLD calculation for most of the period we consider, in a region where barrier layer is known to be thick during that season (Qu and Meyer 2005, Mignot et al. 2007). This is further confirmed by the interannual evolution of MLD calculated using a density criterion over the recent years (red curves on Figure 6). While there is generally a very good agreement between MLD variations estimated from temperature and density criteria (Fig. 6a-c), the MLD variations based on a density criteria along the Sumatra coast are about 3 time weaker compared to the one inferred from a temperature criteria (Fig. 6d), probably owing to the presence of barrier layer in that region (Masson et al. 2002).

In this section, the model mean MLD has been shown to qualitatively agree with observations at both seasonal and interannual timescales. Maximum interannual variability in the model and observations are indeed found in the same regions, i.e. in the eastern equatorial Indian Ocean, and between the equator and 10°S in the Central Indian Ocean in autumn and winter, in relation with the IOD and ENSO. In addition, modeled and observed year-to-year MLD variations over key regions are in good agreement, with correlations ranging between 0.6 and 0.8.

4. MLD interannual variability in the Indian Ocean and related mechanisms

The data coverage is too sparse to allow a detailed description of MLD interannual variability from observations. The reasonably good agreement between model and observed interannual variability gives us confidence in analysing the model outputs to study interannual MLD variations

in more details, and link them with known climate modes in the Indian Ocean. In section 4.1, we will discuss the relative amplitude of interannual MLD variations against other frequency bands (Intraseasonal, seasonal) and evaluate the contributions of known climate modes to large-scale interannual MLD variations. In section 4.2, we isolate MLD variations associated with the IOD and ENSO, while the influence of the SIOD and monsoon interannual variability is addressed in Section 4.3.

4.1 MLD interannual variations

The Indian Ocean is well known for the large-amplitude of its seasonal cycle, associated with reversing monsoonal circulations (e.g. Schott et al. 2002). But apart from this large amplitude seasonal cycle, very significant variability at the intraseasonal and interannual timescales has also been illustrated from many recent studies (see a review in Schott et al. 2009). Below, we estimate the amplitude of MLD variations in the intraseasonal (10-90 day), seasonal, and interannual (i.e. 90-day low passed non-seasonal and detrended anomalies) frequency bands.

We have already described the MLD seasonal cycle, and find not surprisingly that this signal is very large in the latitude band of the easterlies (10-20°S, ~20-25m of standard deviation), toward mid-latitudes (~30 to 42 m of standard deviation), and in the Arabian Sea (~20 to 30m of standard deviation), where the strong seasonally varying wind forcing is not moderated by a haline stratification, like in the Bay of Bengal. In comparison to this very large seasonal cycle, MLD interannual variability is typically about two to four times smaller, with the exception of the eastern equatorial Indian Ocean and along the Sumatra and Java coast where the amplitude of the interannual MLD variations largely exceed the seasonal cycle. Interannual and intraseasonal MLD variations have roughly the same magnitude, except along the equator where intraseasonal fluctuations are about twice as large (See Figure 7).

The amplitude of interannual MLD variations depicted on Figure 7c can be either the result of large scale interannual atmospheric forcing linked to well-known modes of variability (e.g. ENSO, IOD…) or of the interannual signature of oceanic meso-scale variations. Figure 8a-h illustrates the part of the interannual variability explained by large-scale features (by applying the spatial filtering method described in Section 2c). This figure shows that most of the interannual MLD variability in the northern Indian Ocean is actually an interannual signature of small scale variations, especially along the western coast of the Arabian Sea and to a large extent in the Bay of Bengal. The only exception occurs in the central and eastern Arabian Sea in autumn and winter where a large part of the signal appears to be large-scale. From the equatorial region to 15°S, the large-scale component

represents more than 70% of the interannual MLD variability. There is a large contribution of meso-scale variability to the MLD interannual variability south of 15°S in summer and autumn. The largest contribution of meso-scale eddies are hence not surprisingly found in regions of very strong meso-scale activity (Oman and Somalia upwelling, Bay of Bengal and towards the southern hemisphere subtropics, Chelton et al. 2011).

A multiple linear regression of this large-scale component onto the IOD, ENSO and SIOD indices further allows to roughly estimate the percentage of MLD variance explained together by these three major interannual climate modes affecting the Indian Ocean. Figure 8i-l shows that more than half of the MLD variations in the central Indian Ocean south of the equator, along the coast of Java and Sumatra, around 20°S in winter and in the central and eastern Arabian Sea are explained by these main modes of variability. In contrast, most of the large-scale variability that appears south of 15°S in summer and autumn are unrelated to these climate modes. Because of the strong cross-correlations between the climate indices (see Table 1), we will use a partial regression analysis in the next section to separate the contribution of each of the climate modes to interannual MLD variations.

4.2 IOD/ENSO influences

Since the IOD and ENSO are the most strongly correlated indices (table 1), we will separate their respective signals by performing a partial regression of the MLD variability on these two indices.

It is first obvious from Figure 9 and Figure 10 that MLD interannual signals in the South Central Indian Ocean (SCIO box), along the coast of Sumatra (JSC box), in the South East Indian Ocean (SEIO box) and in the Thermocline Ridge of the Indian Ocean (TRIO box) are largely driven by IOD related forcing rather than ENSO. The SCIO signal is the largest, with a maximum of 6m for a typical IOD event (Figure 10a), and an amplitude exceeding 10m for the largest events (see Figure 6). The typical amplitude of other IOD-related signals is weaker and ranges from 2 to 3m depending on the region considered (Figures 9a-d). The timing of these signals also appears to be different: while the SCIO signal peaks before the IOD (August September) and do not persist after November (Figure 9ab, Fig 10a), the JSC signal is maximum during the IOD peak and lasts longer (Fig. 9bcd, Fig. 10b). The SEIO and TRIO signals develop during the IOD peak and persist for about ~6 months until following spring, well beyond the end of the IOD surface signal (Figs. 9bcd, Figs 10c and 10e). The eastern Arabian Sea in late summer and autumn appears to be the only region dominated by ENSO variations (Figs. 9f and 10d).

The mechanisms explaining these MLD variations can be qualitatively assessed from Figures

11 and 12. These mechanisms largely vary from one place to another. During a positive IOD event, stronger than usual southeast trade winds blow in the southern central and eastern equatorial Indian Ocean throughout the boreal summer and autumn, and increase friction velocity there (Fig. 11a-b). This process largely controls the MLD variations in the SCIO region (Fig. 12a). Along the Java Sumatra coast and in the SEIO region, large buoyancy flux anomalies develop during and after the IOD peak (Fig. 11f-g), probably due to shortwave radiation increase (associated with reduced atmospheric convection) that exceeds the latent heat flux cooling effect. This buoyancy flux anomaly appears to dominate the MLD interannual variability in the JSC (Fig. 12b) and SEIO (Fig. 12e) regions. It is however likely that the Ekman-pumping-induced thermocline deepening in the SCIO and coastal upwelling along the Sumatra coast (Yu et al. 2005, Rao and Behera 2005) also reinforce MLD changes in those areas. In the TRIO region, increased friction velocities associated with the IOD only contribute to the MLD deepening in September - October (Fig. 12c), but buoyancy flux anomalies (Fig. 11fgh) associated with increased convection and reduced solar heat flux then control the MLD (Fig. 12c). In the Eastern Arabian Sea, wind stirring and fluxes appear to play an almost equivalent role in the ENSO MLD shoaling in this region during autumn (Fig 12d, Fig 9f).

4.3 Subtropical dipole and monsoon influences

As indicated by table 1, there is a weak (~ -0.4) correlation between the SIOD and both the IOD and ENSO. In order to extract the signal purely associated with the SIOD, we present below a partial regression to the SIOD index, with the influence of IOD removed. Note that a similar regression, with the influence of the ENSO removed gives very similar results. Since the monsoon interannual variations are highly independent from other climate indices (see table 1), the impact of the monsoon on the MLD can easily be obtained from simple linear regression to the monsoon index.

Figure 13 shows a very clear MLD deepening in most of the tropical Indian Ocean south of 15°S, associated with SIOD positive events. This deepening starts in October (i.e. a few months before the SIOD itself) and finishes in February (Fig. 14a). The subtropical high strengthens and shift south during the SIOD positive phase (Behera and Yamagata 2001), thus inducing stronger winds between 15°S and 25°S (Figure 13b). This results in an increase in the frictional velocity (Fig 13b) and large buoyancy due to latent heat losses (Fig 13c), which both contribute to the MLD deepening (Fig. 14b).

Quite surprisingly, MLD interannual variations associated with monsoon intensity changes appear to be small in the model. Intense monsoons are indeed related with very modest MLD deepening in the central and Eastern Arabian Sea (Figure 15a). These variations are however

strongly related to the variations of the monsoon index (~0.7 correlation). This weak MLD variability in the central-eastern Arabian Sea is further confirmed by our observational dataset where interannual MLD variations hardly exceed 7% of the mean summer MLD depth, with an interannual standard deviation of ~4m (Figure 5a). Regressing the MLD changes in this region to interannual fluctuations of the monsoon index further reveals that monsoon-induced MLD variations are of ~1.6m in the model and ~2m in the observations. This weak MLD interannual variability during summer in the northern Indian Ocean may partly be attributed to the relatively weak year-to-year monsoon wind fluctuations (about 10% of the total signal). As shown on Figure 15bc, these modest MLD changes are largely related to wind stirring (and Ekman pumping) effect rather than buoyancy fluxes.

5. Summary and Discussion

5.1 Summary

The Indian Ocean is home to many important modes of climate variability ("capacitor response" to ENSO, IOD, SIOD, Summer Monsoon), in which air-sea fluxes almost always play an important role (either in promoting the growth of the SST anomaly or damping it). In this respect, the thickness of the mixed layer is an important parameter, because it modulates the propensity of the surface layer to respond to atmospheric fluxes. While the MLD seasonal cycle has been studied in the Indian Ocean (e.g. Rao et al. 1989), there has been no detailed study of its interannual variations. In this paper, we describe MLD interannual variations in the Indian Ocean, and their relations with known climate modes.

Our study relies on both observational and modeling datasets. The observational dataset is built from both hydrographic (1969-2008) and Argo data (2002-2008), where MLDs are estimated directly from individual profiles and is made available at http://www.lodyc.jussieu.fr/cdblod/mld.html. Largest interannual MLD variations are found in autumn and winter with opposite polarities in the eastern equatorial and south-central Indian Ocean, in association with IOD and/or ENSO events. The data coverage is however too sparse (especially over the historical period) to allow a precise description of the MLD interannual variability from observations. An eddy-permitting OGCM simulation is further used to investigate the interannual MLD variations, their relationship with well-known climate modes (IOD, ENSO, SIOD and Monsoon) as well as to qualitatively discuss their driving mechanisms. The model reasonably reproduces the observed MLD climatology, despite some biases in the eastern equatorial region. Maximum interannual variability in the model and observations are found in the same regions and

display similar spatial patterns and reasonable phase agreement (correlation with observations between 0.6 and 0.8). The model analysis reveals that MLD interannual variability has a standard deviation of ~3-10 m, two to four times smaller than seasonal variations, and with an amplitude similar to intraseasonal (90 day and shorter) MLD fluctuations. A large fraction of interannual MLD variations is linked to large-scale climate modes (ENSO, IOD, SIOD), with the exception of coastal and subtropical regions where interannual signature of small-scale structures dominates. The IOD explains most of the MLD interannual variability in the 10°S-10°N band, a positive IOD event being associated with a shoaling of the MLD in equatorial and south eastern Indian Ocean and a deepening in the south-central Indian Ocean. Interannual MLD signature of El Niño events is rather weak, except in autumn in the eastern Arabian Sea where the MLD shoals. Interannual variations of the summer monsoon jet only play a modest role, with limited MLD deepening in the Arabian Sea in summer during strong monsoon years. Finally, positive Indian Ocean Subtropical Dipoles are associated with a MLD deepening between 15°S and 30°S. In most of these regions, the buoyancy fluxes appear to dominate MLD fluctuations, with winds playing a role in a few regions through both stirring and Ekman pumping (e.g. Southern Central Indian Ocean and summer Arabian Sea). A large part of the large-scale MLD interannual anomalies remains unexplained in boreal summer and autumn south of 15°S and in winter in the Arabian Sea.

5.2 Discussion

The most obvious limit of the current study is the observational coverage. Whereas Argo data provides a good spatial coverage to monitor interannual variability over the Indian basin since ~2002, this is not a long enough period to accurately monitor interannual variability of the MLD. The historical XBT and CTD datasets of course offers much more temporal depth but sparse sampling, in particular south of 15°S. In addition, MLD field is heavily influenced by air-sea fluxes, with synoptic variations O(100-1000 km) at timescale of a few days, meaning that isolated measurements can be affected by small spatial and temporal scale “noise”, unrelated to wider climate features.

We have hence chosen a modeling approach to complement the limitations of this observing dataset. But the model is itself susceptible to systematic deficiencies in its formulation and forcing datasets. We did not undertake sensitivity tests to e.g., the forcing dataset or vertical mixing parameterization, but compared the results of this ¼° simulation with those of a 2° resolution version using the same forcing. While MLD variations related to the interannual signature of small-scale structures are considerably larger in the ¼° simulation, both simulations result in highly similar large-scale interannual MLD variations related to climate variability, suggesting that most of the

results described in this study are rather independent of the resolution. But we feel that the best encouragement to trust results in this study is provided by the model validation. Modeled MLD has in general a similar mean state and seasonal cycle (Figs. 2 and 3) than observations, and display similar regions of interannual variability (Figs. 4 and 5). Interannual variations of the model MLD compare reasonably well with available sparse observations in four key-regions (with correlations ranging from 0.6 to 0.8, Figure 6). We hence feel that we can rely on the model and available forcing dataset to describe the interannual variability over a longer period. Note in particular that, while the model forcing is probably quite accurate from 1985 onward (relying on ERA-40 re-analysis and ISCCP shortwave radiations), the model uses climatological incoming shortwave radiation before 1985, which probably induces an underestimation of the MLD variability during this period, by neglecting buoyancy flux variations linked to solar fluxes.

The current study was largely motivated by the potential influence of mixed layer depth variations on interannual variations of SST. Figure 16 attempts to roughly quantify this effect. The term associated with surface heat fluxes in the mixed layer temperature interannual anomaly equation corresponds to: $F_{INT}= (Q/ (\rho C_p h))'$ with Q the net surface heat flux, ρ the seawater density, C_p the seawater volumic heat capacity, h the mixed layer depth (we have neglected penetrating solar heat fluxes in this expression for explanation purposes, but used the full expression in the computations of Fig. 16). The ' symbol designates the computation of interannual anomalies with respect to the mean seasonal cycle. Fig16a shows region where the amplitude of F_{INT} is strong, like for example the eastern equatorial Indian Ocean, coastal and subtropical regions and to a lesser extent the 0-10°S band. In order to estimate the contribution of MLD interannual variations to this term, Fig 16b shows the root mean square difference between F_{INT} and F_{CLIM} divided by the standard deviation of F_{CLIM} where $F_{CLIM}=(Q/(\rho C_p h_c))'$ is the heat flux forcing term of the mixed layer, computed using a climatological seasonal cycle of the MLD h_c rather than the MLD h. This shows that MLD contributes to ~40 to 100% of the amplitude of the atmospheric forcing term in several climatically relevant regions like the eastern IOD pole, the thermocline ridge, the eastern Arabian Sea and the Bay of Bengal.

One of the analyses in this paper (Figure 7) suggests that MLD intraseasonal variability is as large as the interannual variability or larger. This intraseasonal variability is probably partly due to known modes of atmospheric intraseasonal variability like the Madden-Julian Oscillation (Zhang, 2005) or monsoon active / break phases (Goswami, 2004). There are also very clear SST signatures of these modes, which appear to be largely driven by air-sea fluxes in most regions (e.g. Jayakumar et al. 2011, Vialard et al. 2011). Intraseasonal MLD variations associated with those modes may

hence have clear impacts on their SST response. Contrary to interannual signals, Argo data record is long enough to describe MLD intraseasonal variations (see, e.g. the work of Drushka et al. 2011 for boreal winter). In future, we will use a combination of observations and modeling to investigate MLD intraseasonal variability over the Indian Ocean.

Acknowledgements: Keerthi M.G is supported by a Junior Research Fellowship (JRF) from Indian National Centre for Ocean Information Services (INCOIS, MOES, Govt. of India). Jérôme Vialard and Matthieu Lengaigne are funded by Institut de Recherche pour le Développement (IRD). Matthieu Lengaigne contributed to this paper while visiting the National Institute of Oceanography (NIO) in Goa, India. The authors also acknowledge the DRAKKAR project (http://www-meom.hmg.inpg.fr/Web/Projets/DRAKKAR/) for providing the oceanic simulations. This is NIO contribution number xxxx.

References:

Ali MM, Sharma R (1994) Estimation of mixed layer depth in the equatorial Indian Ocean using Geosat altimeter data, Mar Geol, 17**:**63–72.

Annamalaia H, Murtugudae R, Potemra J, Xiea SP, Liu P, Wang B (2003) Coupled dynamics over the Indian Ocean: spring initiation of the Zonal Mode, Deep-Sea Res II, 50: 2305–2330.

Babu KN, Sharma R, Agarwal N, Agarwal VK, Weller RA (2004) Study of the mixed layer depth variations within the north Indian Ocean using a 1-D model, J Geophys Res, 109:1-9.

Barnier B, Madec G, Penduff T, Moilnes JM, Treguier AM, Sommer Le, Beckmann A, Biastoch A, Boning C, Deng J, Derval C, Durand E, Gulev S, Remy E, Talandier C, Theetten S, Maltrud M, McClean J, De Cuevas B (2006) Impact of partial steps and momentum advection schemes in a global ocean circulation model at eddy permitting resolution, Ocean Dyn, 56:543–567.

Behera SK, Yamagata T (2001) Subtropical SST dipole events in the southern Indian Ocean, Geophys Res Lett, 28(2):327–330, doi: 10.1029/2000GL011451.

Bentamy A, Katsaros KB, Alberto M, Drennan WM, Forde EB, Roquest H (2003) Satellite estimates of wind speed and latent heat flux over the global oceans. J Clim 16: 637-656.

Brien O, Hurlburt HE (1974) Equatorial jet in the Indian Ocean: theory, Science, 184: 1075–1077.

Brodeau L, Barnier B, Treguier AM, Penduff T, Gulev S (2010) An ERA40-based atmospheric forcing for global ocean circulation models. Science Direct, 31: 88-104, doi:10.1016/j.ocemod.2009.10.005

Blanke B, Delecluse P (1993) Variability of the tropical Atlantic Ocean simulated by a general circulation model with two different mixed-layer physics, J Phys Oceanogr, 23:1363–1388.

Carton JA, Grodsky SA, Liu H (2008) Variability of the oceanic mixed layer 1960-2004, J Clim, 21**:**1029-1047.

Chelton DB, Schlax MG, Samuelson RM (2011) Global observation of nonlinear mesoscale eddies, Prog Oceanogr, 91:167-216, doi:10.1016/j.pocean.2011.01.002.

Cravatte S, Madec G, Izumo T, Menkes C, Bozec A (2008) Progress in the 3-D circulation of the eastern equatorial Pacific in a climate ocean model, Ocean Modelling, 17:28-48, doi: 10.1016/j.ocemod.2006.11.003

Cleveland RB, William SC, McRae JE, Terpennig I (1990) STL: A Seasonal – Trend decomposition procedure Based on Loess, J Official Statistics,6:3-33.

de Boyer Montegut C, Madec G, Fischer AS, Lazar A, Iudicone D (2004) Mixed layer depth over the global ocean: an examination of profile data and a profile-based climatology. J Geophys Res, 109, C12003, doi: 10.1029/2004JC002378

de Boyer Montegut C, Vialard J, Shenoi SSC, Shankar D, Durand F, Ethé C, Madec G (2007) Simulated seasonal and interannual variability of mixed layer heat budget in the northern Indian Ocean, J Clim, 20:3249–3268.

Drushka K, Sprintall J, Gill ST (2011) In situ observations of Madden-Julian Oscillation mixed layer dynamics in the Indian and western Pacific Oceans, J Clim, in revision.

Du Y, Qu T, Meyers G, Masumoto Y, Sasaki H (2005) Seasonal heat budget in the mixed layer of the south eastern tropical Indian Ocean in a high-resolution global general circulation model, J Geophys Res, 110:C04012, doi:10.1029/2004JC002845

Findlater J (1969) A major low level air current over the Indian Ocean during the northern summer, Quart J Roy Meteor Soc, 95:362–380.

Foltz GR, Vialard J, Praveen Kumar B, McPhaden MJ (2010) Seasonal mixed layer heat balance of the southwestern tropical Indian Ocean, J Clim, 23: 947-965.

Gill AE (1982) Atmosphere-Ocean Dynamics, Academic Press, 662 pp.

Gopalakrishna VV, Sadhuram Y, Ramesh Babu V (1988) Variability of mixed layer depth in the northern Indian Ocean during 1977 and 1979 summer monsoon seasons, IJMS, 17:258-264.

Goswami BN (2004) Interdecadal change in potential predictability of the Indian Summer Monsoon, Geophys Res Lett, 31, L16208, doi: 10.1029/2004GL020337

Gould J, Roemmich D, Wijffels S, Freeland H, Ignaszewky M, Jianping X, Pouliquen S, Desaubies Y, Send U, Radhakrishnan K, Takeuchi K, Kim K, Danchenkov M, Sutton P, King B, Owens B, Riser S (2004) Argo profiling floats bring new era of in situ ocean observations, Eos Trans, AGU, 85(19), 185, doi: 10.1029/2004EO190002.

Hendon H Harry (2003) Indonesian Rainfall Variability: Impacts of ENSO and Local Air–Sea Interaction, J Clim, 16:1775- 1790.

Izumo T, Vialard J, Lengaigne M, de Boyer Montegut C, Behera SK, Luo JJ, Cravatte S, Masson S, Yamagata T (2010) Influence of the state of the Indian Ocean Dipole on the following year's

El Nino, Nature Geoscience, doi: 10.1038/NGEO760

Jackett DR, McDougall TJ (1995) Minimal adjustment of hydrographic profiles to achieve static stability, J Atmos Oceanic Technol, 12:381–389.

Jayakumar A, Vialard J, Lengaigne M, Gnanaseelan C, McCreary JP, Praveen Kumar B (2011) Processes controlling the surface temperature signature of the Madden-Julian Oscillation in the thermocline ridge of the Indian Ocean, Clim Dyn, doi:10.1007/s00382-010-0953-5.

Ju J, Slingo J (1995) The Asian summer monsoon and ENSO, Quart J Roy Meteor Soc, 121:1113-1168

Klein SA, Soden BJ, Lau NC (1999) Remote sea surface temperature variations during ENSO: Evidence for a tropical atmospheric bridge, J Clim, 12: 917–932.

Lengaigne M, Madec G, Menkes C, Alory et G (2003) The Impact of Isopycnal mixing on the Tropical Ocean Circulation. Journal of Geophysical Research, 108, 3345, doi: 10.1029/2002JC001704.

Lengaigne M, Boulanger J-P, Menkes C, Spencer H (2006) Influence of the seasonal cycle on the termination of El Niño events in a Coupled General Circulation Model, Journal of Climate, 19, 1850–1868, doi: 10.1175/JCLI3706.1.

Lengaigne M, Vecchi GA (2010) Contrasting the termination of moderate and extreme El Niño events in Coupled General Circulation Models. Climate Dynamics, doi: 10.1007/s00382-009-0562-3.

Lengaigne M, Haussmann U, Madec G, Menkes C, Vialard J, Molines JM (2011) Mechanisms controlling warm water volume interannual variations in the equatorial Pacific: diabatic versus adiabatic processes, Clim Dyn, DOI 10.1007/s00382-011-1051-z.

Madec G (2008) NEMO, the Ocean Engine. Tech. Rep, Notes de l'IPSL (27), ISSN 1288-1619, Université P. et M. Curie, B102 T15-E5, 4 Place Jussieu, Paris Cedex 5, p. 193

Masson S, Delecluse P, Boulanger J-P, Menkes C (2002) A model study of seasonal variability and formation mechanisms of the barrier layer in the eastern equatorial Indian Ocean, J Geophys Res, 107,8017, doi :10.1029/2001JC000832

McCreary JP, Kundu PK (1989) A numerical investigation of sea surface temperature variability in the Arabian Sea, J Geophys Res, 94:16 097–16 114.

McPhaden MJ, Zebiak SE, Glantz MH (2006) ENSO as an integrating concept in Earth science, Science, 314: 1740-1745.

Mignot J, de Boyer Montegut C, Lazar A, Cravatte S (2007) Control of salinity on the mixed layer depth in the world ocean. Part II: Tropical areas, J Geophys Res, 112, C10010.

Monterey G, Levitus S (1997) Seasonal Variability of Mixed Layer Depth for the World Ocean, NOAA Atlas NESDIS, **14**, 100 pp., Natl. Oceanic and Atmos. Admin., Silver Spring, Md

Murtugudde R, McCreary JP, Busalacchi AJ (2000) Oceanic processes associated with anomalous events in the Indian Ocean with relevance to 1997– 1998, J Geophys Res, 105**:** 3295–3306.

Narvekar J, Prasannakumar S (2006) Seasonal variability of the mixed layer in the central Bay of Bengal and associated changes in nutrients and chlorophyll, Deep-Sea Res I, 53: 820- 835.

Nidheesh, AG, Lengaigne M, Unnikrishnan AS, Vialard J (2011) Decadal variability in the tropical Indo-Pacific region: General Circulation Models analysis, submitted to Climate Dynamics.

Prasad TG (2004) A comparison of mixed-layer dynamics between the Arabian Sea and Bay of Bengal: one-dimensional model results, J Geophys Res, 109**,** C03035, doi: 10.1029/2003JC002000.

Paulson CA, Simpson JJ (1977) Irradiance measurements in the upper ocean, J Phys Oceanogr, 7:953–956.

Qu T, Meyers G (2005) Seasonal variation of barrier layer in the southeastern tropical Indian Ocean, J Geophys Res 110(C11), doi: 10.1029/2004JC002816.issn:0148-0227.

Rao RR, Molinari RL, Festa JF (1989) Evolution of the climatological near-surface thermal structure of the tropical Indian Ocean, J Geophys Res, 94**:** 1081- 10815.

Rao RR, Sivakumar R (2003) Seasonal variability of sea surface salinity and salt budget of the mixed layer of the north Indian Ocean, J Geophys Res, 108, 3009, doi: 10.1029/2001JC000907.

Rao SA, Behera SK (2005) Subsurface influence on SST in the tropical Indian Ocean: Structure and interannual variability, Dyn of Atmos and Oceans, 39:103-135.

Roullet G, Madec G (2000) Salt conservation, free surface, and varying levels: a new formulation for ocean general circulation models, J Geophys Res, 105(C10), 23, 927 942, doi: 10.1029/2000JC900089.

Saji NH, Goswami BN, Vinaychandran PN, Yamagata T (1999) A dipole mode in the tropical Indian Ocean, Nature, 401: 360-363.

Schott F, Dengler M, Schoenefeldt R (2002) The shallow overturning circulation of the Indian Ocean, Prog Oceanogr, 53: 57-103.

Schott FA, Xie SP, McCreary Jr JP (2009) Indian Ocean circulation and climate variability, Rev of Geophys, 47, RG1002/2009

Shenoi SSC, Shankar D, Shetye SR (2002) Differences in heat budgets of the near-surface Arabian Sea and Bay of Bengal: Implications for the summer monsoon, J Geophys Res, 107, doi 10.1029/2000 JC000679.

Sreenivas P, Patnaik KVKRK, Prasad KVSR (2008) Monthly Variability of Mixed Layer over Arabian Sea Using ARGO Data, Marine Geodesy, 31**,** Issue 1, doi : 1080/1490410701812311.

Ummenhofer CC, England MH, McIntosh PC, Meyers GA, Pook MJ, Risbey JS, Sen Gupta A, Taschetto AS (2009) What causes southeast Australia's worst droughts? Geophys Res Lett, 36**,** L04706, doi: 10.1029/2008GL036801.

Vialard J, Menkes C, Boulanger JP, Delecluse P, Guilyardi E, McPhaden M (2001) A model study of the oceanic mechanisms affecting the equatorial SST during the 1997-98 El Niño, J Phys Oceanogr, 31: 1649-1675.

Vialard J, Jayakumar A, Gnanaseelan C, Lengaigne M, Sengupta D, Goswami BN (2011b) Processes of 30-90 day sea surface temperature variability in the Northern Indian Ocean during boreal summer, Clim Dyn, doi: 10.1007/s00382-011-1015-3

Wang C, Picaut J (2004) Understanding ENSO Physics - A Review. In: Earth's climate: the ocean-atmosphere interaction. AGU, Washington D.C., C. Wang, S.-P. Xie and J.A. Carton Eds., 21-48.

Weaver A, Courtier P (2001) Correlation modeling on the sphere using a generalized diffusion equation, Quart J Roy Meteor Soc, 127:1815-1846.

Webster PJ, Yang S (1992) Monsoon and ENSO: Selectively interactive systems, Quart J Roy Meteor Soc, 118:877-926.

Webster PJ, Moore AM, Loschnigg JP, Leben RR (1999) Coupled oceanic atmospheric dynamics in the Indian Ocean during 1997–98, Nature, 401:356–360.

Wyrtki K (1973) An equatorial jet in the Indian Ocean, Science, 181, 262–264.

Xie SP, Yan Du, Gang Huang, Xiao-Tong Zheng, Hiroki Tokinaga, Kaiming Hu, Qinyu Liu (2010) Decadal shift in El Nino influences on Indo-western Pacific and East Asian climate in the 1970s, J Clim, 23:3352-3368.

Yamagata T, Behera SK, Luo JJ, Masson S, Jury MR, Rao SA (2004) Coupled Ocean-Atmosphere variability in the Tropical Indian Ocean, Earth's climate: The Ocean-Atmosphere Interaction, Geophysical Monograph Series 147, Eds. by Wang, C., S.-P. Xie, and J.A. Carton.

Yu W, Xiang B, Liu L, Liu N (2005) Understanding the origins of interannual thermocline variations in the tropical Indian Ocean, Geophys Res Lett, 32, L24706, doi: 10.1029/2005GL024327.

Zhang YC, Rossow WB, Lacis AA, Oinas V, Mishchenko MI (2004) Calculation of radiative fluxes from the surface to top of atmosphere based on ISCCP and other global data sets: refinements of the radiative transfer model and the input data, J Geophys Res, 109, 27.

Zhang C (2005) Madden-Julian Oscillation, Rev Geophys, 43, RG2003, doi: 10.1029/2004RG000158

Figure captions:

Fig 1: **(a)** Total number of profiles per month over the 1969-2009 period. Number of profiles per year in 2° by 2° boxes for **(b)** the hydrographic dataset during the historical period (1969-2002) and **(c)** the Argo dataset for the recent period (2002-2009).

Fig2: **(a)** Climatological MLD derived from the hydrographic dataset using temperature criteria overlaid by climatological wind stress from QuikSCAT. **(b)** Same from Argo dataset using density criteria. (**c)** Same for model MLD (density criteria) and wind stress. Units are in meters for MLD and $N.m^{-2}$ for wind stress.

Fig 3: MLD seasonal anomalies inferred from Argo dataset (density criterion) overlaid with QuikSCAT wind stress seasonal anomalies for **(a)** spring (MAM), **(b)** summer (JJA), **(c)** autumn (SON) and **(d)** winter (DJF), **(e-h)** Same for model. Seasonal anomalies are calculated as the long term average for each season minus long-term mean. Units are in m for MLD and $N.m^{-2}$ for wind stress.

Fig 4: Coefficient of variance of MLD interannual anomalies derived from the hydrographic dataset over the 1969-2007 period for **(a)** spring (MAM), **(b)** summer (JJA), **(c)** autumn (SON) and **(d)** winter (DJF). **(e-h)** Same for model. Regions with less than 13 seasonal observed values (one third of the total number of year in the datasets) are masked. Coefficient of variance are calculated as the MLD standard deviation divided by its mean and expressed in percentage.

Fig 5: MLD anomalies associated with anomalous Indian Summer monsoon years in summer (JJA) derived from **(a)** the hydrographic dataset and **(b)** model. **(c-d)** Same for IOD in fall (SON). **(e-f)** Same for ENSO in winter (DJF). Anomalies are computed as half of the difference between strong (resp. positive) and weak (resp. negative) monsoon (resp. ENSO/IOD) years. Strong and weak Indian Summer Monsoon years are defined according to Webster and Yang (1992) Monsoon index. Definitions of positive and negative IOD and ENSO years follow Ummenhofer et al. (2009) classification. Time series of average MLD anomalies with in the boxes drawn on this figure are shown in figure 6. Regions where observed values are available for less than 4 events (one third of the total number of years used in the composite) are masked.

Fig 6: MLD interannual anomalies derived from hydrographic profiles (temperature criteria, dotted line), Argo profiles (density criteria, red thick line) and model (plain line) averaged over (**a)** Eastern Arabian Sea (see box in Fig. 5ab) in summer (JJA), (**b)** the Southern Central Indian Ocean (see box in Fig. 5cd) in fall (SON), (**c)** the Thermocline Ridge of the Indian Ocean (see box in Fig. 5ef) in winter (DJF) and **(d)** along Java Sumatra Coast (see box in Fig. 5ef) in

winter (DJF). Blue (resp. red) bands highlight weak (resp. strong) monsoon years in panel (a), positive (resp. negative) IOD years in panel (b) and El Niño (resp. La Niña) years in panels (c-d). Weak and strong Indian Summer Monsoon years are derived from Webster and Yang (1992)Monsoon index. Definitions of IOD and ENSO years follow Ummenhofer et al. (2009) classification.

Fig 7: Standard deviation of model MLD at **(a)** Intraseasonal (10-90 day), **(b)** seasonal and **(c)** interannual (90 day and longer non-seasonal anomalies) timescales. Contours on panel a (resp. panel c) show the ratio of intraseasonal (resp. interannual) against seasonal MLD standard deviation (contours every 0.5, with a dashed contours for 0.5). Units are in m for MLD.

Fig 8: Standard deviation of interannual MLD anomalies (in meters) for **(a)** Summer (JJA), **(b)** fall (SON), **(c)** winter (DJF) and **(d)** spring (MAM). **(e-h)** Standard deviation of large-scale (> 250 km) MLD interannual anomalies (in meters) for each season. **(i-l)** Percentage of the large-scale interannual MLD variance explained collectively by IOD, ENSO and SIOD for each season.

Fig 9: Partial regression coefficient of MLD interannual variations (color shading) and of large-scale MLD interannual variations (contour) in **(a)** summer (JJA), **(b)** autumn (SON), **(c)** winter (DJF) and **(d)** spring (MAM) onto IOD index with ENSO influence removed. **(e-h)** Same but for MLD regressed onto the ENSO index with IOD influence removed. Regression coefficients are computed over the 1960-2007 period. Partial regression coefficients for MLD interannual variations are only plotted when they are significant at the 90% confidence level. Contours for large-scale MLD interannual variations are -5, -1, 1 and 5. The boxes plotted on this figure are used in the analyses of Fig. 10 and 12: SCIO (South Central Indian Ocean), SEIO (South East Indian Ocean), JSC (Java Sumatra Coast), TRIO (Thermocline Ridge of Indian Ocean) and EAS (Eastern Arabian Sea). Units are in m.

Fig 10: Seasonal evolution of partial regression coefficients of MLD interannual variations with respect to IOD (blue line) and ENSO (red lines) indices, in the regions outlined in Fig. 9. Bold lines indicate partial regression coefficients that are significant at the 90% confidence level.

Fig 11: Partial regression coefficient of cubic friction velocity interannual variations (color shading), wind stress interannual variations (vector) and large-scale MLD interannual variations (contours) in **(a)** summer (JJA), **(b)** autumn (SON), **(c)** winter (DJF) and **(d)** spring (MAM) onto IOD index, with ENSO influence removed. Partial regression coefficient of buoyancy fluxes interannual variations (color shading) and large-scale MLD interannual variations (contours) in **(e)** summer (JJA), **(f)** autumn (SON), **(g)** winter (DJF) and **(h)** spring

(MAM) onto the IOD index, with the ENSO influence removed. The sign of the buoyancy flux is reverted on panels (e-h) to ease comparison with MLD variations. Regression coefficients are computed over the 1960-2007 period. Partial regression coefficients for MLD interannual variations are only plotted when they are significant at the 90% confidence level. Units are in $m^3.s^{-3}$ for cubic frictional velocity, $N.m^{-2}$ for wind stress, $mg.m^{-2}.s^{-1}$ for buoyancy fluxes and m for MLD. Contour intervals for the MLD partial regression coefficients are -5, -1, 1 and 5m (dotted contours for negative values).

Fig 12: Seasonal evolution of partial regression coefficient of MLD interannual variations (m) onto normalized surface buoyancy flux (blue) and friction velocity (red) for the regions outlined on Figure 9. The sign of the buoyancy flux is reverted to ease comparison with MLD variations. Bold lines indicate partial regression coefficients that are significant at the 90% confidence level.

Fig 13: Partial regression coefficients on to the SIOD index with IOD influence removed of **(a)** MLD interannual variations (color shading) and large-scale MLD interannual variations (contours) in winter (DJF), (**b)** friction velocity interannual variations (color shading), wind stress interannual variations (vectors) and large-scale MLD interannual variations (contours) in winter (DJF) and (**c)** buoyancy fluxes interannual variability (color shading) and large-scale MLD interannual variations (contours). The sign of the buoyancy flux is reverted to ease comparison with MLD variations. Regression coefficients are computed over the 1960-2007 period and are only plotted when they are significant at the 90% confidence level. Units are in $m^3.s^{-3}$ for cubic frictional velocity, $N.m^{-2}$ for wind stress, $mg.m^{-2}.s^{-1}$ for buoyancy fluxes and m for MLD. Contour intervals for the MLD partial regression coefficients are -5, -1, 1 and 5m (dotted contours for negative values).

Fig 14: Seasonal evolution of partial regression coefficient of MLD interannual variations (m) in the SIOD box (plotted in Fig. 13a) **(a)** onto IOD (blue) and the subtropical dipole (red) indices and **(b)** onto normalized buoyancy (blue) and friction velocity (red). The sign of the buoyancy flux is reverted to ease comparison with MLD variations. Bold lines indicate partial regression coefficients that are significant at the 90% confidence level.

Fig 15: Simple regression coefficient onto the Monsoon index in summer (JJA) of **(a)** MLD interannual variations (color shades) and large-scale MLD interannual variations (contours), of (**b)** friction velocity interannual variations (color shades), wind stress interannual variations (vectors) and large-scale MLD interannual variations (contours), and of (**c)** buoyancy fluxes

interannual variability (color shades) and large-scale MLD interannual variations (contours). The sign of buoyancy fluxes is reverted to ease comparison with MLD variations. Regression coefficients are computed over the 1960-2007 period and are only plotted when they are significant at the 90% confidence level. Units are in $m^3.s^{-3}$ for cubic frictional velocity, $N.m^{-2}$ for wind stress, $mg.m^{-2}.s^{-1}$ for buoyancy fluxes and m for MLD. Contour intervals for the MLD partial regression coefficients are -5, -1, 1 and 5m (dotted contours for negative values).

Fig 16: (**a)** Standard deviation of interannual anomalies of the atmospheric surface heat flux forcing term of the mixed layer (in $^oC.month^{-1}$). **(b)** Relative importance of MLD variations (in percentage) in interannual variations of the mixed layer surface heat flux forcing (see text for details).

Table captions:

Table 1: Correlation between the Indo-Pacific modes of variability discussed in this study: IOD and ENSO indices are highly correlated, while monsoon index is weakly correlated with the other modes. The percentage of significance associated with each correlation is shown in brackets.

Figure 1

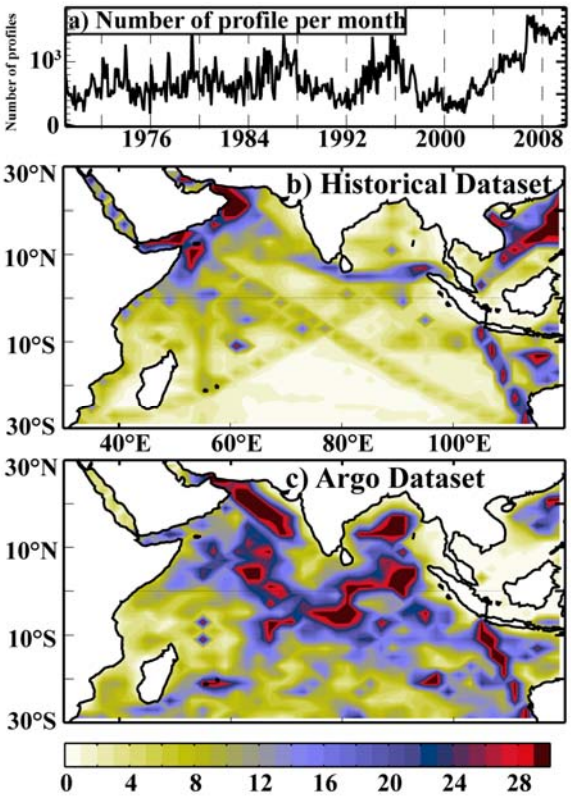
a) Number of profile per month
Number of profiles
10³
0
1976
1984
1992
2000
2008
b) Historical Dataset
30°N
10°N
10°S
30°S
40°E
60°E
80°E
100°E
c) Argo Dataset
30°N
10°N
10°S
30°S
0
4
8
12
16
20
24
28

Figure 2

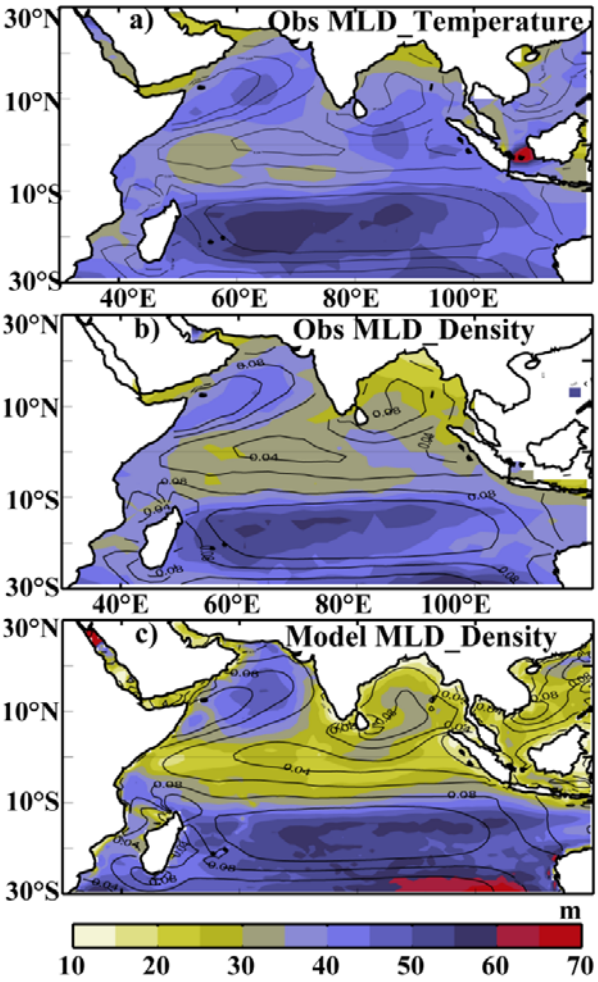
a) Obs MLD_Temperature
b) Obs MLD_Density
c) Model MLD_Density
30°N
10°N
10°S
30°S
40°E
60°E
80°E
100°E
m
10
20
30
40
50
60
70

.

Figure 3

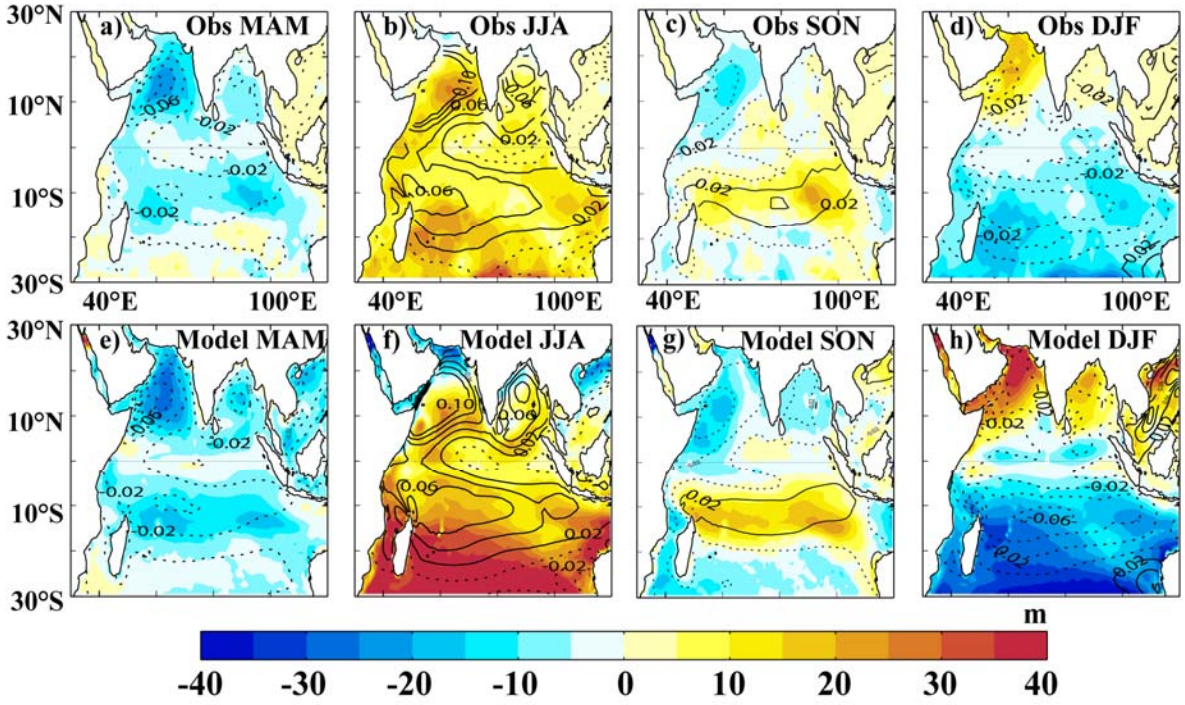

Figure 4

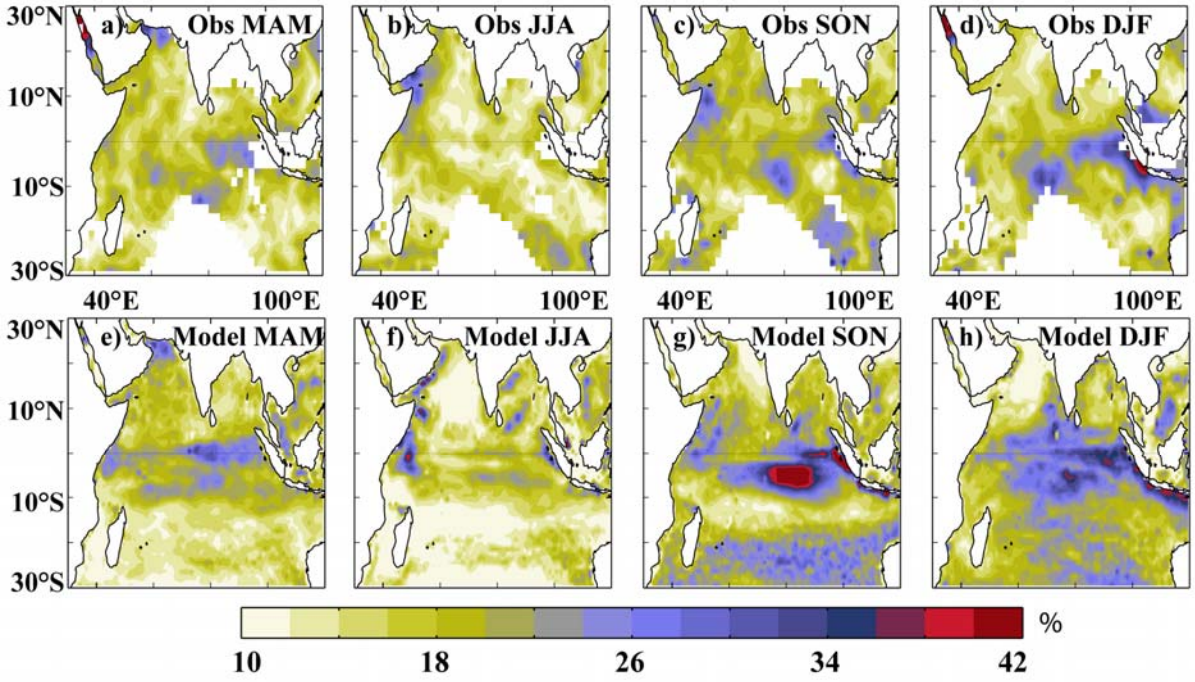

Figure 5

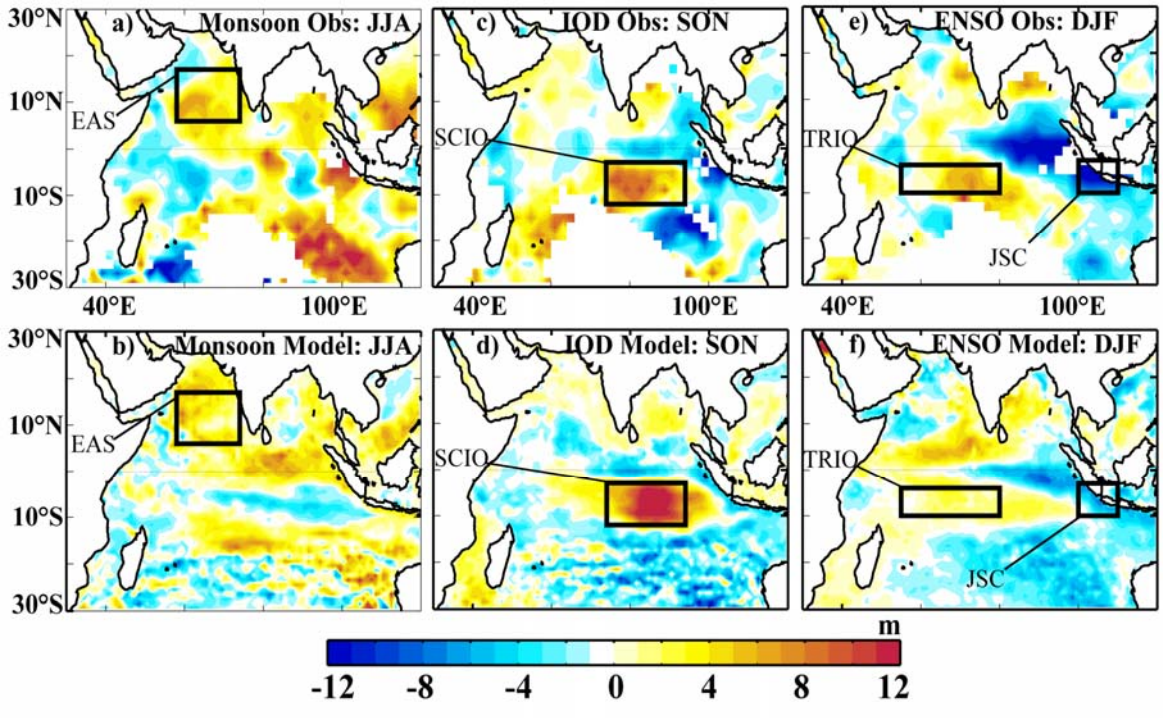

Figure 6

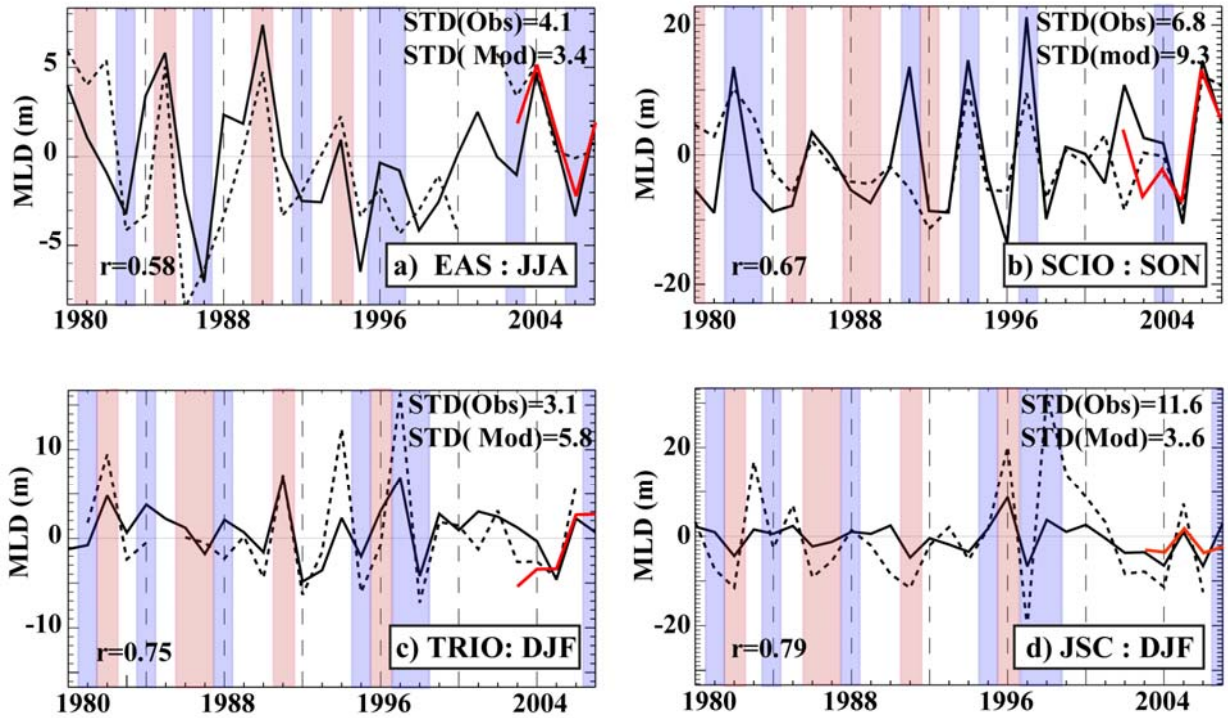

Figure 7

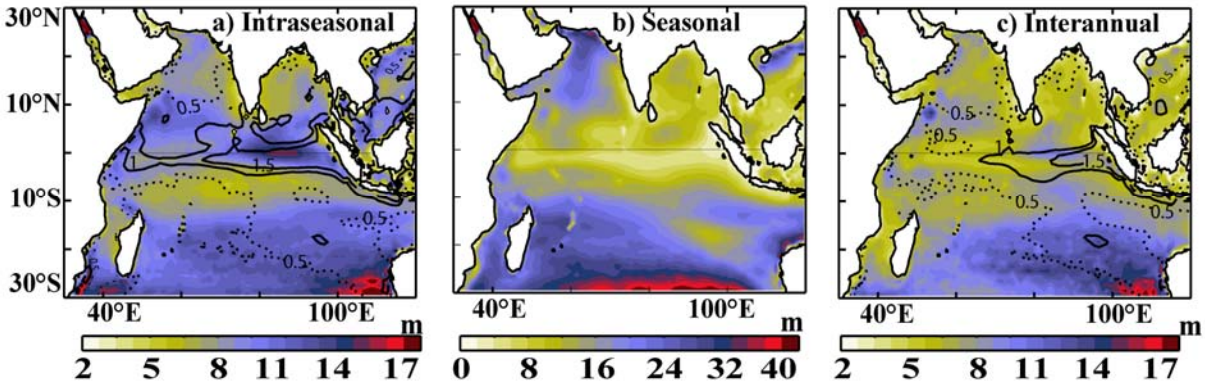

Figure 8

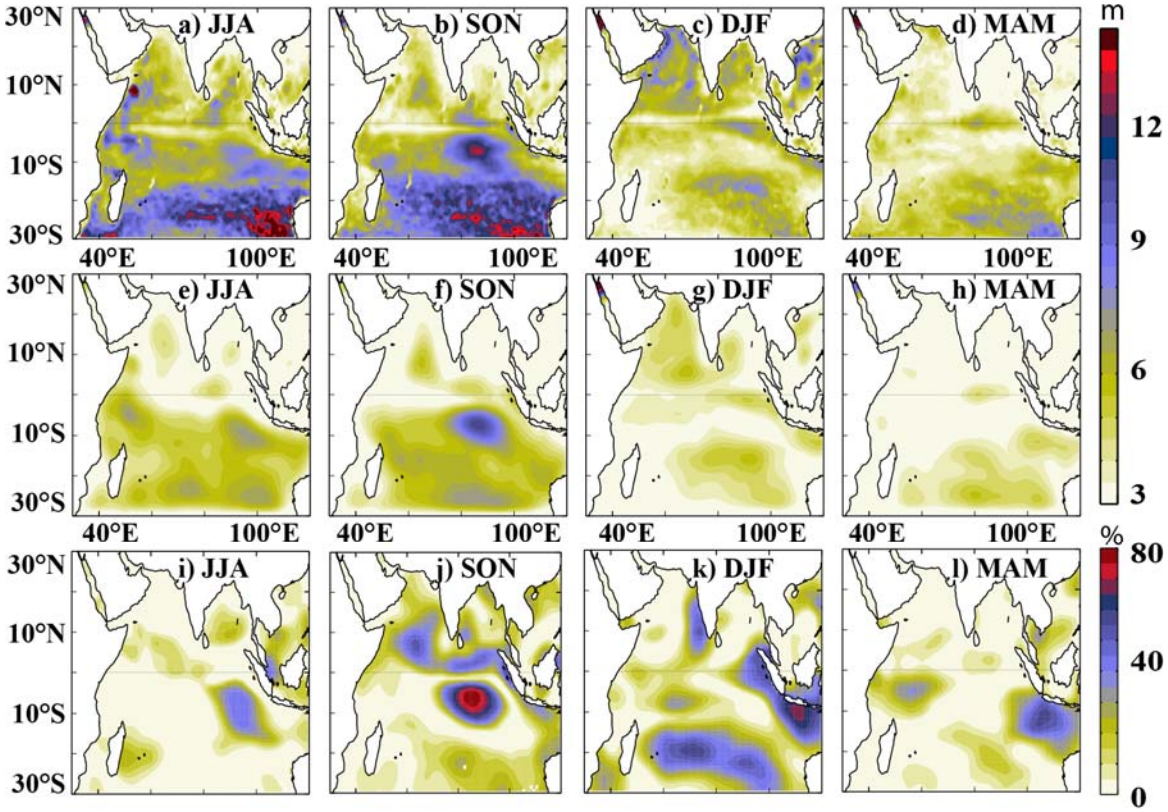

Figure 9

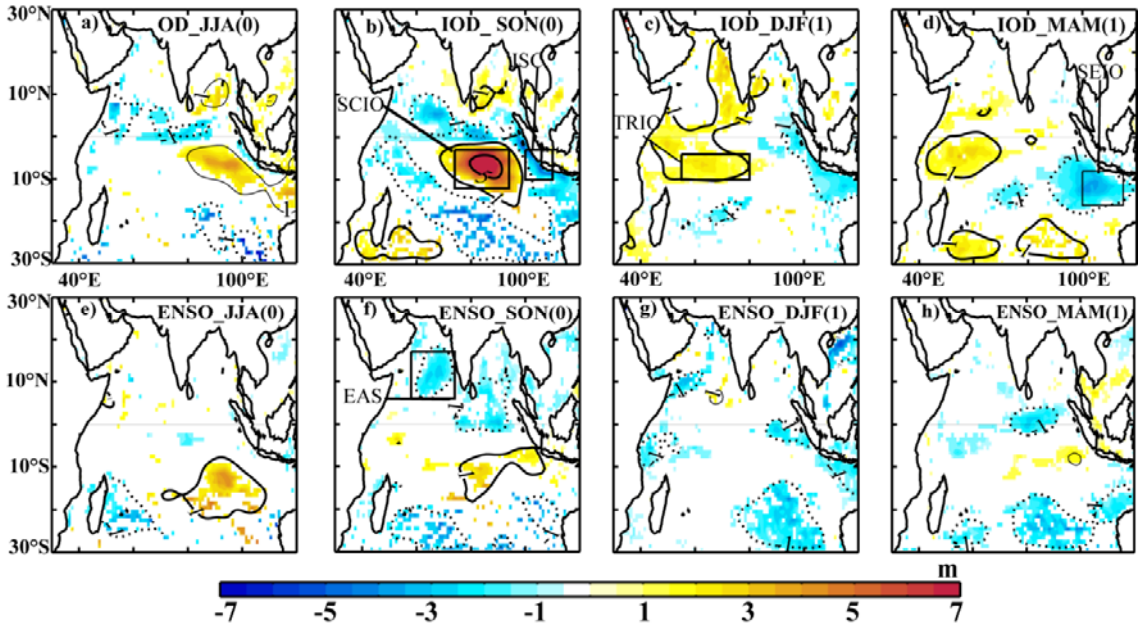
a) OD_JJA(0)
b) IOD_ SON(0)
c) IOD_DJF(1)
d) IOD_MAM(1)
e) ENSO_JJA(0)
f) ENSO_SON(0)
g) ENSO_DJF(1)
h) ENSO_MAM(1)
SCIO
ISC
TRIO
SEIO
EAS
30°N
10°N
10°S
30°S
40°E
100°E
m
-7
-5
-3
-1
1
3
5
7

Figure 10

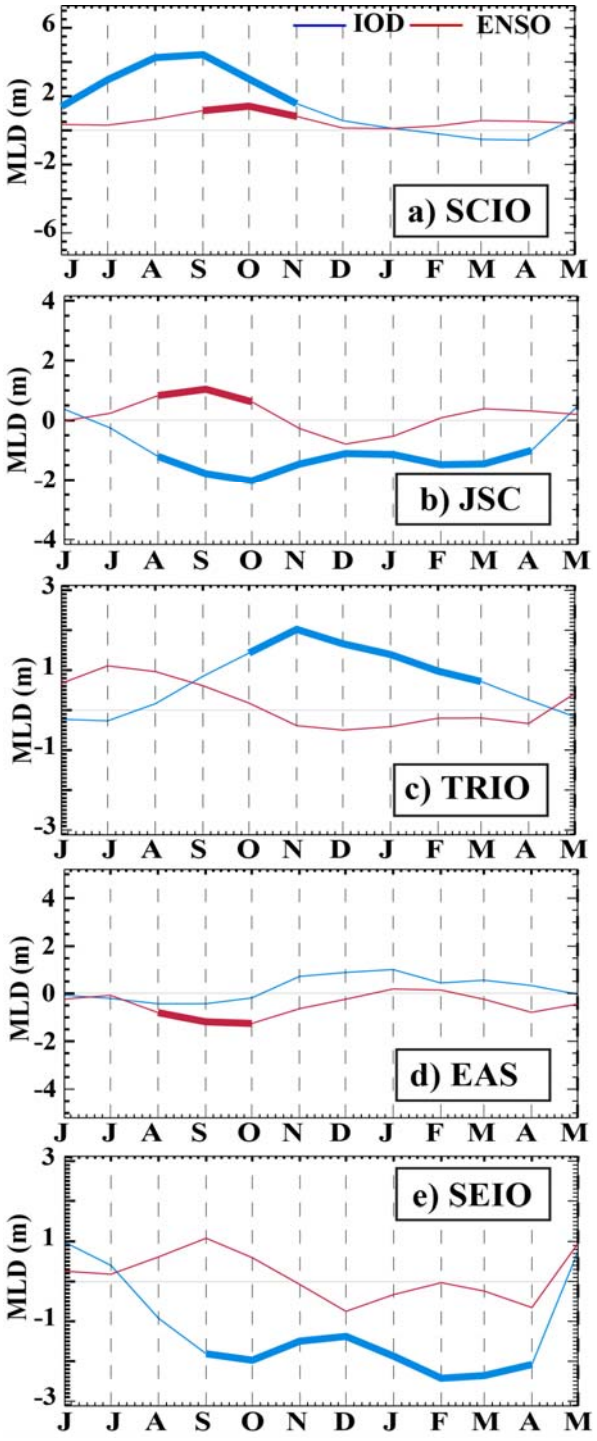

Figure 11

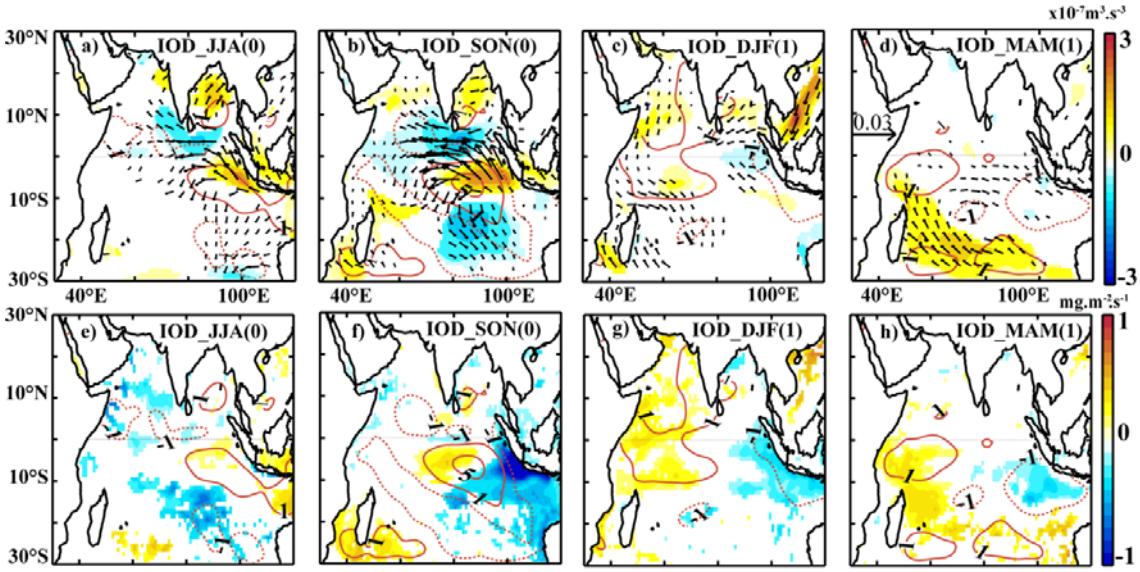
a) IOD_JJA(0)
b) IOD_SON(0)
c) IOD_DJF(1)
d) IOD_MAM(1)
e) IOD_JJA(0)
f) IOD_SON(0)
g) IOD_DJF(1)
h) IOD_MAM(1)
30°N
10°N
10°S
30°S
40°E
100°E
0.03
x10⁻⁷m³.s⁻³
3
0
-3
mg.m⁻².s⁻¹
1
0
-1

Figure 12

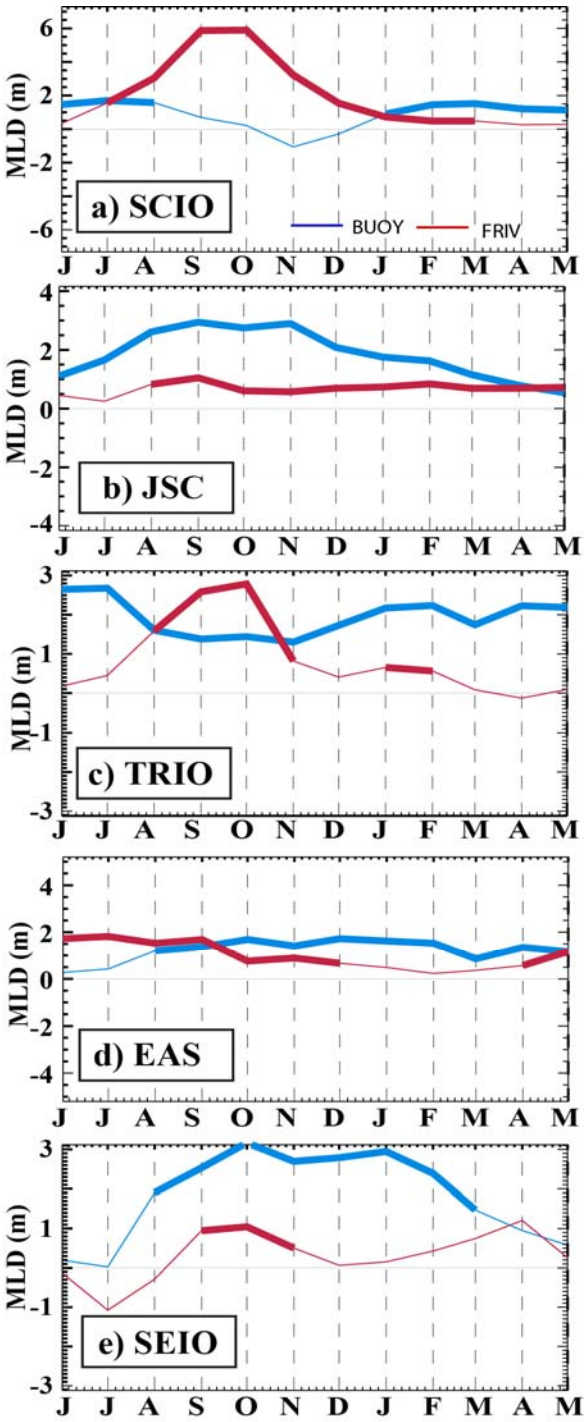

Figure 13

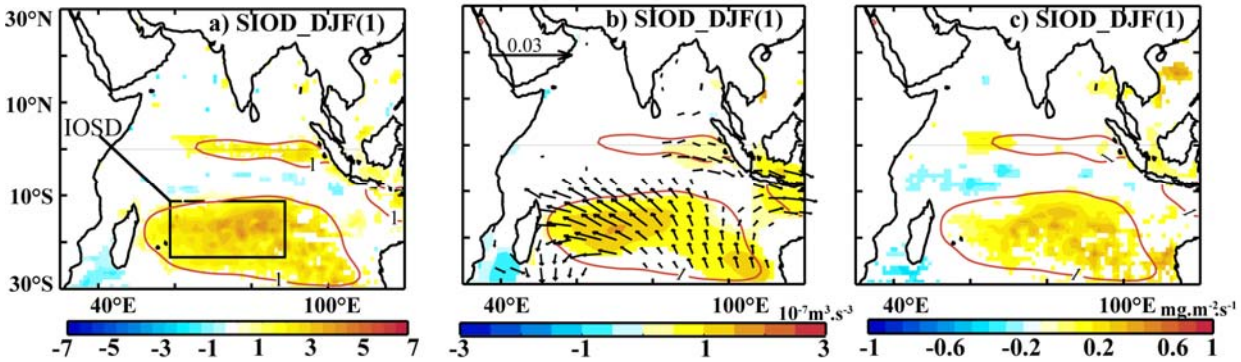

Figure 14

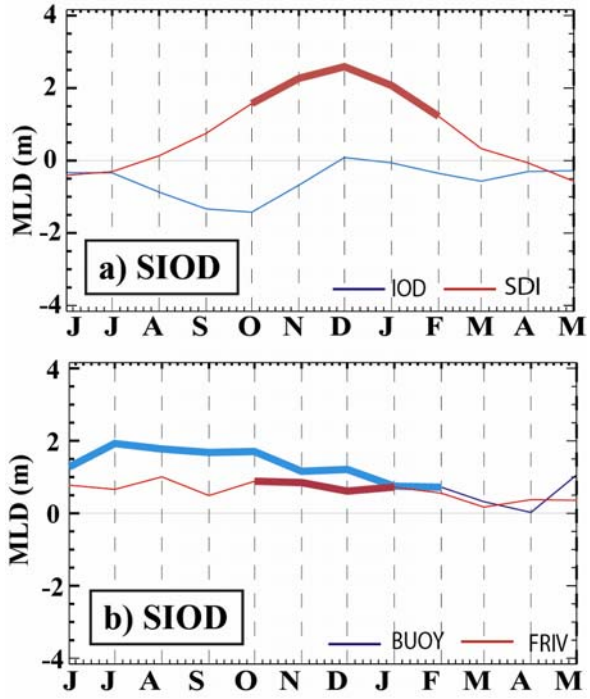

Figure 15

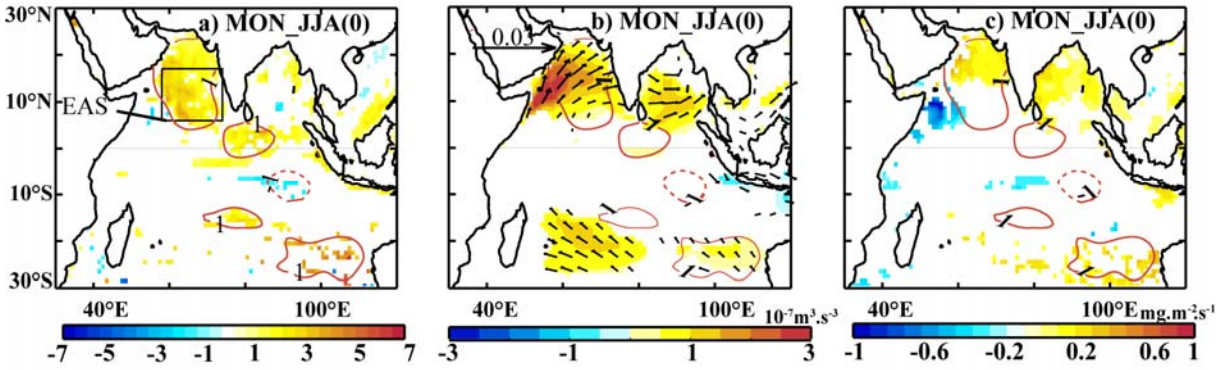

Figure 16

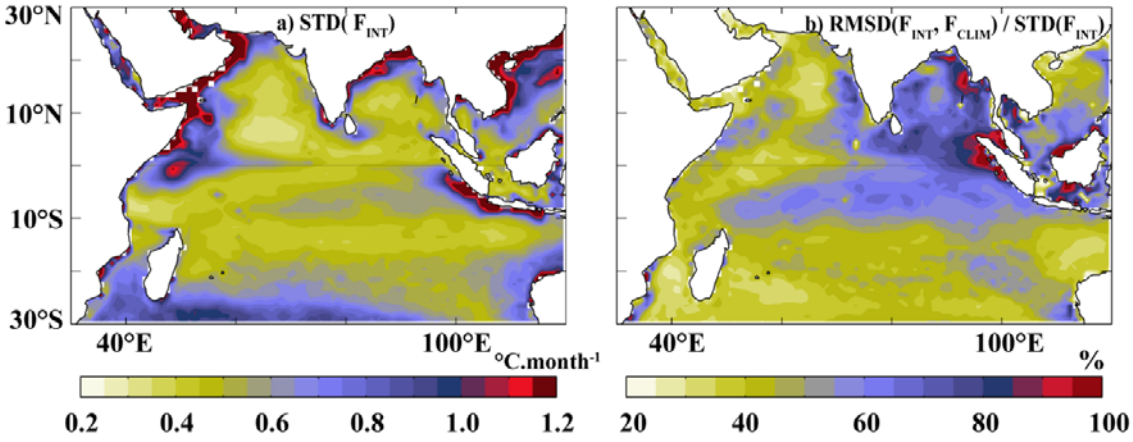

Table 1:

	ENSO	SIOD	MON
IOD	**0.70(100)**	**-0.44(100)**	**-0.24(91)**
ENSO		**-0.40(100)**	**-0.27(95)**
SIOD			**0.26(93)**